


In the format provided by the authors and unedited.

# Coherent storage and manipulation of broadband photons via dynamically controlled Autler-Townes splitting

Erhan Saglamyurek<sup>1\*</sup>, Taras Hrushevskiy<sup>1</sup>, Anindya Rastogi<sup>1</sup>, Khabat Heshami <sup>2</sup>  
and Lindsay J. LeBlanc <sup>1,3\*</sup>

---

<sup>1</sup>Department of Physics, University of Alberta Edmonton, Alberta, Canada. <sup>2</sup>National Research Council Canada, Ottawa, Ontario, Canada. <sup>3</sup>Canadian Institute for Advanced Research, Toronto, Ontario, Canada. \*e-mail: [saglamyu@ualberta.ca](mailto:saglamyu@ualberta.ca); [lindsay.leblanc@ualberta.ca](mailto:lindsay.leblanc@ualberta.ca)

# Supplementary Material: Coherent storage and manipulation of broadband photons via dynamically controlled Autler-Townes splitting

Erhan Saglamyurek,<sup>1</sup> Taras Hrushevskiy,<sup>1</sup> Anindya Rastogi,<sup>1</sup> Khabat Heshami,<sup>2</sup> and Lindsay J. LeBlanc<sup>1,3</sup>

<sup>1</sup>*Department of Physics, University of Alberta Edmonton, Alberta T6G 2E1 Canada*

<sup>2</sup>*National Research Council Canada, 1200 Montreal Road Ottawa, Ontario K1A 0R6, Canada*

<sup>3</sup>*Canadian Institute for Advanced Research, Toronto, Ontario M5G 1M1, Canada*

## SI. Cold atom preparation

Our experiments are performed in an apparatus designed for (and capable of) producing Bose-Einstein condensates (BECs) of  $^{87}\text{Rb}$ . For these proof-of-concept demonstrations of the ATS memory, we use atoms from the first stages of this process, immediately following the initial laser cooling stages of a magneto-optical trap (MOT).

Our apparatus consists of a diffusive oven of Rb atoms, which are first mildly collimated into a 2-dimensional MOT chamber, where they undergo cooling along two transverse directions. The resulting atom beam is guided through 15 cm of differential pumping into a final ultrahigh vacuum chamber ( $\approx 10^{-12}$  Torr) made of a borosilicate glass cell. Here, the atoms are collected and cooled in a standard six-beam MOT operating with a red-detuning of  $\approx 3\Gamma$ . The laser frequencies used for cooling match the standard D2 transitions  $|F = 2\rangle \rightarrow |F' = 3\rangle$  for the laser cooling and  $|F = 1\rangle \rightarrow |F' = 2\rangle$  for a “re-pump” beam (Fig. S1). While the frequency of the re-pump laser is servo-locked to the  $|F = 1\rangle \rightarrow |F' = 2\rangle$  line using saturation absorption spectroscopy, the frequency of the cooling laser is stabilized by beat-note locking to the repump laser. After 15 seconds of laser cooling, we collect  $2.0\text{-}2.5 \times 10^8$  atoms in  $|F = 2\rangle$ . At this stage, the MOT magnetic field and the repump beams are switched off, but the cooling laser beams are kept on. After a 4 ms wait, which ensures that the mechanical shutter for the repump beam is completely closed, the cooling laser beams are turned off. This process (leading to an off-resonant pumping via the cooling beams) transfers the atoms from  $|F = 2\rangle$  to  $|F = 1\rangle$ , which serves as the ground level for signal field in the storage experiments. After this transfer, the number of atoms that remains in  $|F = 2\rangle$  is measured to be only  $\sim 3 - 4\%$  of the initial population. Following an additional 3 ms of wait-time (yielding  $\sim 7$  ms of time-of-flight in total), which ensures that residual magnetic field from the MOT is further reduced, the cold atoms are then subjected to the memory read and write beams for storing and retrieving a signal field. Time-of-flight measurements of this cloud yield a size of 3.2 mm diameter ( $1/e^{1/2}$  diameter from Gaussian fit). The peak optical depth is determined to be 4 to 4.5 from an absorption imaging measurement on  $|F = 2\rangle \rightarrow |F' = 3\rangle$  after pumping the atoms back into  $|F = 2\rangle$ .

Future experiments will test the ATS memory in sub-

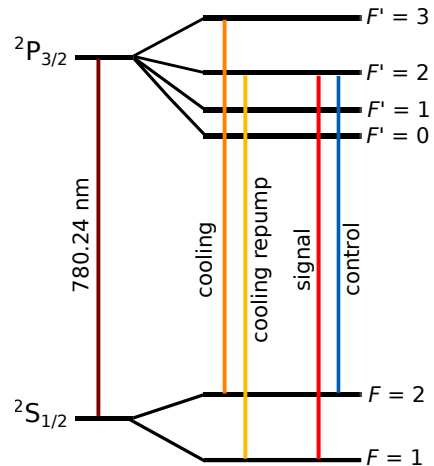


FIG. S1: **Rubidium 87 level structure.** Relevant laser transitions labelled, left-to-right: Bare D2 transition is 780.24 nm; cooling transition used for MOT; repump cooling transition used for MOT; signal transition  $|F = 1\rangle \rightarrow |F' = 2\rangle$ ; control transition  $|F = 2\rangle \rightarrow |F' = 2\rangle$

sequent stages of cooling these atoms in optical trap and eventually in BEC.

## SII. ATS memory setup and measurements

In our experiments, the signal ( $|F = 1\rangle \rightarrow |F' = 2\rangle$ ) and control ( $|F = 2\rangle \rightarrow |F' = 2\rangle$ ) fields are derived from the cooling repump beam (an extended cavity diode laser) and a tunable titanium sapphire laser (Fig. S1), respectively. The frequency of each laser is independently servo-locked to the corresponding D2 transition with a  $-80$  MHz detuning using saturation absorption spectroscopy. The continuous-wave (cw) signal field is first gated by an acousto-optic modulator (AOM) that introduces a frequency shift of  $-80$  MHz. Then, it is sent to another AOM in double-pass configuration that generates resonant signal pulses with  $\tau_{\text{FWHM}} = 30\text{--}70$  ns by shifting the frequency  $+160$  MHz. This AOM is also used for ms-long frequency-swept signal pulses with a  $\pm 20$  MHz scan range to spectrally characterize ATS. The cw control field is passed through an AOM that produces resonant write and read-out pulses with 30 to 70 ns duration at FWHM and a  $+80$  MHz frequency shift. In

the memory setup, the AOMs for the signal and control pulses are driven by amplified RF oscillators that are amplitude controlled by a two-channel arbitrary-waveform generator (AWG) with a 250 MS/s sampling rate. In the interference measurements, the signal pulses are instead generated using a single-pass AOM with detuning of +80 MHz, and both the signal and control AOMs are directly driven by AWG with larger sampling rate (2 GS/s) that allows preparation of signal pulses with the desired phase.

After setting the frequency, phase, and amplitude of the signal and control fields, each beam is separately coupled to a polarization-maintaining fiber with an output at the cold-atom apparatus. The beams are launched toward the 3D-MOT chamber with fiber-decoupling lenses that collimate the beams with mm-scale waists. The polarization of the each beam (initially linear) is controlled by quarter-wave (QWP) plates, for providing the maximum interaction strength between the fields and atoms. Following the QWPs, the signal and control beams are combined on a 50/50 beamsplitter and overlapped inside the atomic cloud with Gaussian beam diameters ( $1/e^2$ ) of 2.3 mm and 3.0 mm and the separation angle of  $2^\circ$ , respectively. The peak power of the signal before the cloud is typically 30  $\mu$ W for storage experiments with large mean photon numbers ( $\bar{n}_{\text{in}} \gg 1$ ) and less than 100 nW for ATS characterization. The peak power of the control field before the cloud is between 0.5 mW and 15 mW, depending on the experiment. After interacting with the cold atoms, the signal is coupled to a single-mode fiber for an additional spatial filtering from the strong control field. This yields, in total, 65 – 70 dB isolation, which provides no measurable leak from the control to the signal in the storage experiments with  $\bar{n}_{\text{in}} \gg 1$ . Finally, the signal is directed to a fast photo-detector (Resolved Instruments DPD80, 100 MHz bandwidth) or a slow-detector with large sensitivity (4 MHz bandwidth) for storage or spectral measurements, respectively. In addition to the signal, a small fraction of the control beam that is reflected off a 5/95 beam splitter is coupled to a fiber and detected to enable synchronization with the signal, as well as to calibrate the power.

### Spectral measurements

For spectral measurements to characterize the natural line and ATS lines of the ( $|F = 1\rangle \rightarrow |F' = 2\rangle$ ) transition, a 1 ms frequency-swept signal with power of  $\mathcal{P}_{\text{in}}(\Delta)$  and linearly varying detuning ( $\Delta(t)$  from -20 MHz to +20 MHz) is sent to the atomic cloud, and the transmitted signal  $\mathcal{P}_{\text{out}}(\Delta)$  is detected to determine the absorption with respect to  $\Delta$  in terms of optical depth:  $d' = \ln(\mathcal{P}_{\text{in}}/\mathcal{P}_{\text{out}})$ . The measured absorption profiles allow us to directly determine the transition linewidth  $\Gamma^{\text{exp}}$  (for  $\Omega_c = 0$ ) and ATS spacing  $\delta_A^{\text{exp}} \approx \Omega_c$  (for  $\Omega_c > \Gamma$ ). This is achieved by fitting each absorption peak trace to a Lorentzian function. Although this measurement

should also determine the peak optical depth (at  $\Delta = 0$ ), it has yielded  $d^{\text{exp}} = 2.3 - 2.7$  for the natural transition line, which is about 25% less optical depth compared to an estimation from the imaging measurement, due to a partial destruction of the cloud during interaction. When the sweep range is changed to the detuning range -4 MHz to +36 MHz, this degradation is significantly less, yielding peak optical depth of  $d^{\text{exp}} \approx 3.1$ . To further confirm, the natural transition line is probed with a resonant pulse with  $\sim 0.5 \mu$ s duration and 30  $\mu$ W (yielding less power delivery per spectral interval). The measured peak optical depth is  $d^{\text{exp}} \approx 3.3$  with some fluctuations due to laser frequency jitter.

### Memory measurements

In a typical storage experiment with  $\bar{n}_{\text{in}} \gg 1$ , a short signal pulse and a write field are simultaneously sent to the atomic cloud. After a pre-set storage time controlled by the AWG, a read-out field is generated for retrieval. The detected time series of the retrieved and transmitted (non-absorbed part of the input) signals are recorded on an oscilloscope. To avoid potential degradation of the cloud by several signal pulses, only one signal pulse is stored and retrieved per cooling cycle. This measurement cycle is typically repeated 3-5 times and the data is averaged to improve the signal-to-noise ratio. The area under the curve of power vs. time is determined for the output (retrieved) signal and compared to the input signal (measured in the absence of atoms), using Gaussian fits to the data (which are generally well fit). The ATS memory efficiency ( $\eta^{\text{exp}}$ ) is determined from the ratio of the retrieved area to the input area. For a given memory configuration (with certain bandwidth and storage time), the memory efficiency exhibited variations up to  $\pm 15\%$  due to instabilities in atom number (optical depth) and spin-wave decoherence time, and up to  $\pm 10\%$  and  $\pm 5\%$  drift of the power of input signal and control fields, respectively, on the minute-to-minute timescale.

### Phase-sensitive measurements

In our experiments, the interference measurements demand a fixed phase relationship between the control and signal fields, which is not guaranteed by the measurement procedure described above, where each field is derived from independent lasers and also carried over meters-long fiber-optic patchcords. To overcome this limitation, we send a stream of pulse quartets – an input signal pulse (each encoded with different relative phase), a reference signal pulse (to be interfered with each recalled signal), and two control pulses (each with the same phase) – to the atomic cloud to effect storage and retrieval. Several of these quartets are sent in less than 5  $\mu$ s, with varying input signal pulse phases in each quartet, which ensures that there is no significant phase drift between each stor-

age/recall due to the short time scale. We confirmed that each signal pulse experiences the same absorption, by observing that no measurable destruction of the cloud is observed before the last pulse quartet. Furthermore, in order to avoid any cross-talk, additional read-out pulses are applied between each storage/recall quartet, guaranteeing that any spin coherence left from the storage of the previous input and reference signal is removed for the next interference measurement.

Under these conditions, the phase of each retrieved signal  $\theta'_s$  is determined by three contributions: (i) the phase of the input signal  $\theta_s$ , (ii) the accumulated phase during the evolution of spin-wave  $\theta_{sw}$  for a given storage time, and (iii) the phases of the write and read-out  $\theta_c$ , yielding  $\theta'_s = \theta_s + \delta\theta$ , where  $\delta\theta = \theta_{sw} + \theta_c$  is the overall phase imparted in storage and retrieval, which is controllable via  $\theta_c$ . As described in the main article, the phase of the reference pulses  $\theta_r$  is set to be fixed, and also their amplitude and duration are adjusted to be the same as the retrieved signal. Thus, the intensity of the interfering recalled signal and reference pulse depends on only  $\theta_s$  with respect to  $\theta_r$ , assuming the memory introduces the same  $\delta\theta$  unitary phase transformation for every  $\theta_s$  with a fixed  $\theta_c$  and storage time. Two such interference measurements are illustrated in Fig. 4a of the main article (lower panel) for  $\Delta\theta = \theta_s - \theta_r = 0$  and  $\Delta\theta = \pi$  with an observation of near-perfect constructive and destructive interference, respectively, showing that  $\delta\theta = 0$  for each  $\theta_s$ , and thus the relative phase is preserved in the memory. For further confirmation, as presented in Fig. 4b of the main article,  $\theta_s$  is varied from  $0^\circ$  to  $360^\circ$  in steps of  $45^\circ$  and the resulting intensity measurements ( $I$ ) yield an interference visibility  $V = (I_{\max} - I_{\min}) / (I_{\max} + I_{\min}) = 89 \pm 6\%$  and  $V = 98 \pm 2\%$  for  $\delta\theta = 0$  (black square) and  $\delta\theta = \pi$  (red circle), determined by fitting each data set to a sinusoidal function, respectively.

### Single-photon level measurements

For the single-photon level measurements ( $\bar{n}_{\text{in}} < 1$ ), two main modifications are done in the setup described above. First, in order to reduce the light from the control beam that leaks into the signal field's spatial mode, the angle of the control beam with respect to the signal beam is increased from  $2^\circ$  to  $75^\circ$ . This improves the isolation of the control from 70 dB to 140 dB, whereas the memory efficiency drops to about 5% from the typical efficiency of 7% for 200 ns storage time. We attribute this reduction mainly to spatial mismatch between the signal and control fields that leads to non-optimal spin-wave mapping. Second, we heavily attenuate the number of photons contained in our 40 ns-long signal pulses down to the single-photon level using neutral density filters just before the MOT cell. We detect these single-photon level pulses using a fiber-pigtailed silicon avalanche photo-diode (Si-APD) unit with 50% detection efficiency and 200 dark counts per second. The optical input and

electronic output of the detector are connected to the memory fiber-optic coupler and either a digital counter or a time-to-digital converter (TDC), respectively. The detector is electronically gated only at those time intervals in which signal pulses are sent for measurements, and also protected by a mechanical shutter to avoid excessive number of stray photon detections during the cold atom preparation.

We determine the average number of photons per signal pulse  $\bar{n}$  by measuring the number of signal photon detections  $n_d$  with respect to the number of generated signal pulses  $n_p$  over the same time interval and in the absence of atomic cloud (MOT). Provided that  $\bar{n} = n_d/n_p < 0.1$  (yielding negligibly small probability of detecting multiphoton per pulse according to Poissonian statistics), the mean photon number before memory is given by  $\bar{n}_{\text{in}} = (1/\eta_t) \times \bar{n}$ , where  $\eta_t \approx 0.1$  is the detection probability of a signal photon, given by the detector efficiency and transmission loss from the memory output to the single photon detector. To cross-check these numbers, we compare this directly measured  $\bar{n}_{\text{in}}$  to the one calculated from the attenuation factors of the neutral density filters and peak power of signal pulses just before the filters. We find a good agreement between these values.

In the single-photon-level memory demonstrations, we establish the input mean photon number to be  $\bar{n}_{\text{in}} = 0.3$  per  $\tau_{\text{FWHM}} = 40$  ns-long signal pulse. We send a sequence of these signals, comprising 1000 pulses separated by  $1 \mu\text{s}$  spacing, to the memory for storage and retrieval for each preparation of atomic cloud. For collecting reliable statistics, this prepare/measure cycle is repeated 500 times, yielding in total  $n_p = 5 \times 10^5$  storage/recall attempts. For each storage/recall event, the arrival times of the detected photons are resolved by the TDC, allowing measurement of detection counts for the transmitted and retrieved signals separately, as shown in Fig. 4c of the main article. We measure the total detection counts for the recalled signal to be  $n_d = n_p \bar{n}_{\text{in}} \eta_t \eta = 722 \pm 30$  (where  $\eta$  is the memory efficiency) by summing the number of recorded detections in the time-bins over a 60 ns interval centered on the midpoint of the recalled signal. We establish the contribution of the noise detections to be  $n_n = 17 \pm 4$  counts by performing the same  $n_p = 10^5$  measurements in the absence of signal pulses, yielding an unconditional noise detection probability  $p_n = (n_n/n_p) \times (1/\eta_t) \approx 3 \times 10^{-4}$ . From these measurements, we determine the ratio of the recalled signal to noise to be  $\text{SNR} = (n_d - n_n)/n_n = 40 \pm 10$ . We further investigate the origin of this residual noise by performing the same measurement in the absence of signal pulses and atomic cloud, while the control fields are on. This measurement gives the same number of noise counts  $n_n = 17 \pm 4$ . Finally, we measure the total number of counts coming from the detector dark counts and the detections of ambient photons to be  $4 \pm 2$ , when the signal, control and MOT are all off. This confirms, within the statistical error, that the residual noise floor arises

mainly from the stray control photons, and there is no measurable four-wave mixing contribution to the noise for our experimental conditions.

### SIII. Optimization, calibration and alignment procedures for experiments

We follow various preparation procedures for our experiments as detailed below. First, the positions of the signal and control beams are aligned with respect to the atomic cloud using strong resonant fields that remove atoms from the interacting section of the cloud. This section is monitored using absorption imaging on a CCD camera, and the beams are aligned until a reasonable overlap is obtained. Second, the control field peak power is regularly calibrated by comparing a set of actual power measurements before the atomic cloud with the ones measured from the monitor detector. Third, the polarization of the control and signal beams is optimized by maximizing both peak absorption and peak spacing of the ATS  $\delta_A$  (measured with the transmission of a frequency-swept signal) for a given control field power. Fourth, for the pulsed-ATS memory demonstrations, the synchronization between the signal and the control pulses was carried out by monitoring signals from the respective detectors, which are positioned with equal optical distance from the atomic cloud. When required, the relative delay is tuned by introducing a trigger delay to the AWG channels. Fifth, in order to optimize spin coherence time, the residual magnetic field at the cloud location is compensated to near-zero using three pairs of bias coils that can independently produce uniform DC magnetic fields in each of the three dimensions. This procedure was carried out by maximizing the efficiency of the memory with iterative adjustments of the bias magnetic fields. Finally, atom number (optical depth) is optimized day-to-day by optimizing laser-cooling parameters.

### SIV. Performance of our ATS memory implementation

In our proof-of-principle demonstrations of an ATS memory, our typical sequence uses an input signal with bandwidth  $B_{\text{FWHM}} = 11$  MHz ( $\tau_{\text{FWHM}} = 40$  ns). This signal is stored for  $T = 200$  ns and retrieved with  $\eta^{\text{exp}} = 7 - 8\%$  efficiency in the forward direction. By adapting Eq. 15 to our experimental configuration, the memory efficiency is determined by  $d_A$  (peak optical depth of ATS lines),  $F_{\text{eff}}$  (effective ATS factor that takes into account additional broadening in the ATS lines), and decay-time constant  $T_d$  for a given storage time  $T$  due to spin-wave decoherence, giving

$$\eta^{\text{exp}} \approx (d_A/2F_{\text{eff}})^2 e^{-d_A/2F_{\text{eff}}} e^{-1/F_{\text{eff}}} e^{-T/T_d}. \quad (\text{S1})$$

We determine  $T_d$  experimentally by extending the storage time up to  $1.0 \mu\text{s}$  and measuring the memory effi-

ciency for different storage times in this range, as shown in Fig. S.II. From measurements performed at different times, we find that  $T_d$  is typically  $(330 \pm 13)$  ns, but can be as low as  $(220 \pm 15)$  ns depending on the bias-magnetic-field optimization. These measurements also find the spin decoherence rates in our system as  $\gamma_s^{\text{exp}}/2\pi = 1/2\pi(2T_d) \approx 0.24$  to  $0.4$  MHz. In the ideal case ( $\gamma_s = 0$  and no extra ATS line broadening), as treated with Eq. 15 in the main article, the peak optical depth of the ATS lines is the same as the measured peak optical depth of the transition line ( $d_A = d^{\text{exp}}$ ), and the width of each ATS line is  $\Gamma_{\text{ATS}} = \Gamma^{\text{exp}}/2$ , which defines  $F_{\text{eff}} = \Omega_c/(2\Gamma_{\text{ATS}}) = \Omega_c/\Gamma^{\text{exp}}$ . In practical settings, when the spin-decoherence rate ( $\gamma_s$ ) is comparable to the polarization decay rate ( $\gamma_e$ ) and/or the control Rabi frequency (which determines the ATS splitting) is not uniform across the medium, then the ATS peaks become wider and lower. This effect can be analyzed using an experimentally obtained ATS spectrum, which is shown in Fig. 3c of the main article for our typical setting  $\Omega_c/2\pi \approx 11$  MHz. From this spectrum we measure the linewidth of each ATS peak at FWHM is to be  $\Gamma_{\text{ATS}}^{\text{exp}}/2\pi \approx 1.5 \times (\Gamma^{\text{exp}}/2)/2\pi \approx 6.0$  MHz for  $\Gamma^{\text{exp}}/2\pi \approx 7.7$  MHz (the measured transition linewidth including residual Doppler broadening), which yields  $F_{\text{eff}} = F/1.5 \approx 1$ . Similarly we find that the peak optical depth is reduced with approximately the same factor, yielding  $d_A \approx d^{\text{exp}}/1.5 \approx 2.3$  for our measured peak optical depth  $d^{\text{exp}} = 3.5$ .

We further investigate the origin of the observed line broadening of  $\delta\Gamma_{\text{ATS}}/2\pi = (\Gamma_{\text{ATS}}^{\text{exp}} - 0.5 \times \Gamma^{\text{exp}})/2\pi \approx 2$  MHz for  $\Omega_c/2\pi \approx 11$  MHz. In order to find the contribution from the spin decoherence effect, we simulate the absorption profiles of the ATS system using the generic susceptibility expression for a three-level system for the measured spin-decoherence rates ( $0.24$  to  $0.35$  MHz) and the control Rabi frequency ranges ( $\Omega_c/2\pi \leq 17$  MHz) used in the experiments. We establish this contribution to be in the range of  $\approx 0.20 - 0.30$  MHz, which is, in most cases, negligibly small due to the fact that  $\gamma_s \ll \gamma_e$  is satisfied in our experiments. Therefore, the major contribution to the ATS broadening comes from the spatial non-uniformity of the control Rabi frequency over the interaction cross-section of the atomic gas, which leads to position-dependent ATS splitting that manifests as broadening in their spectra. In our experiment, this non-uniformity originates from the similar beam sizes of the overlapping control and signal fields, each with gaussian intensity profiles in diameters of  $3.0$  and  $2.3$  mm, respectively. To further confirm, we characterize the degree of the ATS line broadening as a function of the power of the control field. We observe that the broadening increases proportionally to the square root of the power ( $\delta\Gamma_{\text{ATS}} \propto \sqrt{\mathcal{P}}$ ), and for relatively high power values ( $\mathcal{P} > 5$  mW) the spectrum of each ATS line is predominantly characterized by a Gaussian spectral profile, indicating the inhomogeneous nature of the broadening due to varying ATS splittings. In the general treatment of a

dynamic ATS including this effect, the power dependence of the broadening as well as the alteration in the ATS spectra, which accordingly modifies the definitions of  $F$  and  $\tilde{d}$ , need to be taken into account. For the cases that  $\delta\Gamma_{\text{ATS}}/2 \ll \Omega_c$ , as in our implementation whose overall efficiency has degraded about 30% due to this broadening effect, treatment of an effective line broadening (reducing  $F$ ) with nearly preserved effective optical depth is a reasonable approximation, as the system dynamics are still mainly governed by the mean  $\Omega_c$ .

Consequently, using the experimentally extracted parameters of  $d_A = 2.3$ ,  $F_{\text{eff}} = 1$  and  $T_d = 300$  ns in Eq. S1 gives a predicted memory efficiency of 8% which is in agreement with the directly measured memory efficiency of  $\eta^{\text{exp}} = 7 - 8\%$ .

Beyond our proof-of-principle demonstration, there are clear paths to substantially improve the performance of our ATS memory implementation in terms of efficiency, storage time, and bandwidth as detailed in the next section.

### SV. Limitations and potential improvements in our ATS memory implementation

The main limitation in our experiments is a fast spin-decoherence rate, which degrades the efficiency and the storage time. This limitation is mainly due to residual magnetic fields, leading to dephasing between the atoms that are populating different Zeeman sublevels. The slow switch-off time of the MOT coils is one source of this residual field, which is not totally compensated by the DC-bias fields. One way to overcome this issue in the current setup is to implement polarization-gradient cooling (optical molasses), which would extend the time after switching off the MOT fields before storage and retrieval, and would additionally increase the optical density. In conjunction with microwave or RF spectroscopy, which systematically allows the measurement and, therefore, cancellation of residual fields, it should be possible to optimize the spin-coherence time from the current value of a few-hundred nanoseconds to a few-hundred microseconds, as demonstrated in several experiments with cold atoms [S1, S2]. The other factor limiting the efficiency is the small optical depth, which can be significantly increased with polarization gradient and evaporative cooling. Moreover, as our apparatus is capable of producing ultracold atoms in an optical dipole trap, more than an order of magnitude improvement in optical depth is within our reach. In combination with sufficiently large coherence times, this improvement should lead to the memory efficiency larger than 50% with the backward-propagation scheme. Finally, in our current setup, the memory bandwidth is technically limited by our electronics and AOMs, which give the shortest pulses of  $\tau_{\text{FWHM}} = 30$  ns ( $B_{\text{FWHM}} \approx 15$  MHz), and by the peak Rabi frequency  $\Omega_c/2\pi \approx 20$  MHz. As the Rabi frequency depends on the power and beam diameter, reducing the

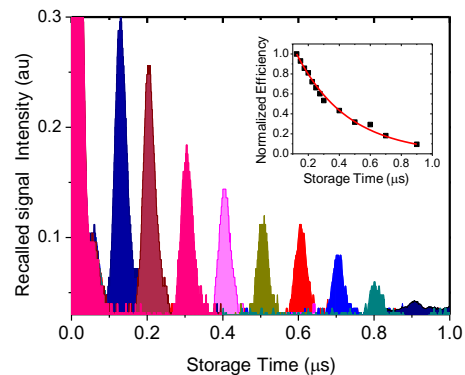


FIG. S2: **Retrieved signal intensity with respect to storage time.** An input signal with  $\tau_{\text{FWHM}} = 40$  ns is stored and retrieved up to a microsecond. The decay arises from spin-wave decoherence, whose main source is non-zero ambient magnetic fields that lift degeneracy of the Zeeman levels and lead to dephasing between the spin states. The inset shows a fitting of the normalized memory efficiency to a decaying exponential function, which yields decay time of  $(330 \pm 13)$  ns

beam diameter from the current 3 mm to 0.3 mm (with the corresponding change of the signal beam size), we can obtain Rabi frequencies of 200 MHz, which, in principle, should allow 200 MHz memory bandwidth. On the other hand, as the spacing between the adjacent D2 excited levels is only on the order of 100 MHz, such a broadband memory scheme would not be possible with D2. An alternative solution to this limitation is to employ the D1 line in  $^{87}\text{Rb}$  which has about 800 MHz spacing between its excited levels. Together with sufficiently large optical depths, such an implementation should allow a few-hundred MHz bandwidth in our current setup. Finally, we point out that the ATS line broadening due to the non-uniform Rabi frequencies, as observed in our experiments, can be easily eliminated by appropriate selection of the beam sizes, for instance, choosing the control beam size much greater than the probe size.

### SVI. Numerical analyses and simulations of experiments

The numerical analyses of the Maxwell-Bloch equations are performed with a standard Euler method using MATLAB software. Before calculations, the consistency of the atom-light parameters ( $d$ ,  $\gamma_e$  and  $\Omega_c$ ) with respect to their definitions is inspected. First, by considering  $\Omega_c = 0$ , the response of the two-level system ( $|g\rangle$  and  $|e\rangle$ ) is probed by a test signal pulse for an example setting of  $\Gamma^{\text{set}} = 2\gamma_e^{\text{set}}$  and  $d^{\text{set}}$ . The bandwidth of the test signal is chosen to be much smaller than  $\Gamma^{\text{set}}$ . Under these conditions, the output signal arising from a zero-detuning input signal is numerically calculated. From the attenu-

ation of the test signal, the optical depth is found to be  $d = d^{\text{set}}$ , exactly as defined. In addition, this examination is performed for test signals with detunings from  $-4\Gamma$  to  $+4\Gamma$ . For each detuning, the output is calculated, and absorption is plotted with respect to detuning. The resulting Lorentzian curve has a linewidth of  $\Gamma/2\pi = \Gamma^{\text{set}}/2\pi$  at FWHM, exactly as defined. Second, the dynamics of the three-level system is inspected for a test control field in the regime  $\Omega_c > \Gamma$ . In this case, the input test signal's bandwidth is chosen to be larger than  $\Omega_c^{\text{set}}$ , and the time dependence of spin, photon and polarization are calculated. As expected from the theory, it is verified that each component oscillates exactly at the period of  $\Omega_c/2\pi = \Omega_c^{\text{set}}/2\pi$ .

The simulation of the storage experiments is performed using the measured atom-light parameters  $d^{\text{exp}}$ ,  $\Gamma^{\text{exp}}$  and  $\Omega_c$  (extracted from independent experiments), and the recorded input and control field traces, which contain all timing information of the experiment and control power. The Rabi frequency for the control field is calibrated according to  $\Omega_c(t)/2\pi = \alpha\sqrt{\mathcal{P}(t)}$  with  $\alpha = 5.75 \text{ MHz}/\sqrt{\text{mW}}$ , which is established from the ATS vs. control power characterizations. In addition, the non-uniformity of the Rabi frequency, resulting in broadened ATS lines ( $\delta\Gamma_{\text{ATS}}$ ) needs to be considered, otherwise the numerically calculated memory efficiency is approximately 25 – 30% more than the directly measured one, while the dynamics are unchanged. This effect is taken into account with a simple model based on our experimental conditions, including  $\gamma_s \ll \gamma_e$ ,  $\delta\Gamma_{\text{ATS}}/2 \ll \Omega_c$  and  $B_{\text{FWHM}} \approx \Omega_c/2\pi$ . As detailed in Section S.IV, under these conditions the overall impact of the ATS line broadening is to reduce the memory efficiency by inducing a larger polarization decay rate (i.e. decreasing  $F$ ), while the effective optical depth ( $\tilde{d}$ ) is approximately preserved. Also by considering that the measured transition width ( $\Gamma^{\text{exp}}$ ) includes a residual Doppler broadening, we define the atom-light coupling rate, the effective polarization decay rate  $\gamma_e^{\text{eff}}$ , and the effective peak optical depth  $d^{\text{eff}}$  as  $g\sqrt{N} = \sqrt{r}d^{\text{eff}}\gamma_e c/2L$ ,  $\gamma_e^{\text{eff}} = (\Gamma^{\text{exp}} + 2\delta\Gamma_{\text{ATS}})/2$ , and  $d^{\text{eff}} = d^{\text{exp}}(0.5 \times \Gamma^{\text{exp}})/\gamma_e^{\text{eff}}$  where  $r = \gamma_e^{\text{eff}}/\gamma_e$ , and  $\delta\Gamma_{\text{ATS}} = \Gamma_{\text{ATS}}^{\text{exp}} - (\Gamma^{\text{exp}}/2)$  is the effective ATS line broadening (excluding the residual contribution from the spin-decoherence), which is extracted from the measured ATS spectra.

As a consistency check, we compare the results of basic experiments configured for  $\Omega_c = 0$  (where there is no ATS memory) to numerical simulations with these parameters. In the first experiments, a long pulse with  $B_{\text{FWHM}} \ll \Gamma^{\text{exp}}/2\pi$  is sent to the cold atoms and the transmitted signal is recorded. These experiments are well simulated in terms of both the profile and amplitude of the transmitted signal using  $d^{\text{exp}} \approx 3.3$  to 3.5. In the second experiments, a short pulse with  $B_{\text{FWHM}} > \Gamma^{\text{exp}}/2\pi$  is sent to the cold atoms. In addition to an attenuated transmission, a coherently emitted delayed pulse due to a stimulation effect is recorded. The shape, amplitude and delay between the re-emission and transmis-

sion are governed by  $d$  and  $\gamma_e$ , allowing their inspection together. These experiments are also well-simulated with setting of  $d^{\text{exp}} \approx 3.3$  and  $\Gamma^{\text{exp}}/2\pi = 2\gamma_e^{\text{eff}}/2\pi = 7.7 \text{ MHz}$  confirming the consistency of our set parameters. Finally, for the storage experiments, the spin-wave decay rate parameter ( $\gamma_s^{\text{exp}}$ ) is extracted from the memory efficiency vs. storage time measurements as described in Section S.IV. The consistency of this parameter is directly verified by simulating each measurement result from the memory efficiency vs. storage time experiment.

Consequently, taking into account the overall instabilities in atoms numbers (optical depth) and spin-coherence times in the day-to-day operation of our system, we set  $d^{\text{exp}} = 3 - 3.5$ ,  $\Gamma^{\text{exp}}/2\pi = 7.7 \text{ MHz}$ ,  $\gamma_s^{\text{exp}}/2\pi = 0.24 - 0.40 \text{ MHz}$ ,  $\delta\Gamma_{\text{ATS}}^{\text{exp}}/2\pi = 1.9 \text{ MHz}$  and  $\Omega_c/2\pi = 5.75 \text{ MHz}/\sqrt{\text{mW}} \times \sqrt{\mathcal{P}}$  in the simulations of all of the experiments.

## SVII. Performance analysis of quantum memory schemes

In the main article, we have compared the performance of the ATS memory scheme to that of the EIT and off-resonant Raman schemes (Fig. 2c-e), based on the criteria detailed in Methods. In this section, we describe the specific details of our numerical analysis for this comparison, including the optimization procedures carried out for each memory scheme.

### ATS memory

For the ATS memory scheme, the calculations are performed for Gaussian input signals using Gaussian-shaped write and read-out control pulses with  $A_c^{\text{write}} = A_c^{\text{read}} = 2\pi$ , as detailed in the main text. Fig. 2a and b show the result of these calculations for ATS memory efficiency vs. optical depth for different  $F$  values in the forward and backward recall schemes, respectively. For the definition of  $F = \Omega_c/\Gamma$  with this dynamic (pulsed) ATS memory,  $\Omega_c$  is effectively equivalent to a constant Rabi frequency that provides the same pulse area ( $2\pi$ ).

In the analyses presented in Fig. 2c for performance comparison, memory efficiency vs. optical depth for the storage and recall of the signal pulse with  $B_{\text{FWHM}} = 13.5\Gamma/2\pi$  ( $\tau_{\text{FWHM}} = 0.1\gamma_e$ ) is calculated in the backward recall configuration with the peak Rabi frequency of  $\Omega_c/2\pi = 1.5B_{\text{FWHM}}$  for write and read-out fields. The memory efficiency exhibits a relatively steep increase in the range of  $d < 100$  (equivalently,  $1 < d\tau_{\text{FWHM}}\gamma_s < 10$ ), and approaches optimal efficiency of  $\eta \approx 0.9$  at  $d \approx 80 - 100$ , yielding  $d\tau_{\text{FWHM}}\gamma_e \approx 8 - 10$ , which agrees with the bounds derived by Gorshkov et al. [S3–S5] for fast memory approaches. (Note that in their notation, optical depth values are twice-larger than the actual values, and the full-width of signal pulses ( $\tau$ ) are used). In addition, as shown with the dashed curve in the same figure, opti-

mal memory efficiency vs. optical depth is established for the ATS scheme. In this analysis, for a given  $d$ ,  $\tau_{\text{FWHM}}$  and  $\Omega_c$  are adapted in such a way that the conditions of  $d\tau_{\text{FWHM}}\gamma_e = 10$  and  $A_c = 2\pi$  are maintained, respectively. Notably, this curve matches the curve that establishes the universal maximum efficiency for any given optical depth independent of memory protocols, analyzed in Ref. [S3].

Data presented in Fig. 2d shows scaling of optical depth with respect to optimal signal bandwidth that provides near-optimal memory efficiency  $\eta > 0.85$ . Similar to the previously described analysis, for a given signal duration  $\tau_{\text{FWHM}} \ll 1/\gamma_e$ , optimal optical depth is determined from the fast operation condition that fulfills  $d\tau_{\text{FWHM}}\gamma_e \approx 8$ . For each  $d\tau_{\text{FWHM}} = 8/\gamma_e$ , it is numerically verified in the range  $B_{\text{FWHM}} = 7\Gamma/2\pi$  to  $110\Gamma/2\pi$  that the efficiency is always maintained as  $\eta \approx 0.85 - 0.95$  with the same system dynamics. In this bandwidth scaling analysis, the peak Rabi frequency of the control fields is changed proportionally to the signal bandwidth in order to maintain the pulse area condition of  $2\pi$ , yielding a curve for peak control power ( $\mathcal{P} \propto \Omega_c^2$  in normalized units) vs. bandwidth, as presented in the inset of Fig. 2d.

Finally, as shown in Fig. 2e, we analyze the ATS memory efficiency vs. spin decoherence rate in the parameter regime very similar to our experimental conditions:  $\tau_{\text{FWHM}} = 40$  ns,  $\Omega_c/2\pi = 16.5$  MHz,  $d = 3.5$ ,  $\gamma_e/2\pi = 3$  MHz and  $\gamma_s/2\pi < 0.5$  MHz. Under these conditions, assuming zero decoherence ( $\gamma_s/2\pi = 0$ ), the efficiency of ATS memory is numerically found to be  $\eta \approx 20\%$ , by satisfying the fast operation condition  $d\tau_{\text{FWHM}}\gamma_e \approx 3$  for the forward recall scheme. Note that this efficiency value is nearly the same as the universal optimal efficiency for  $d = 3.5$  for both forward and backward retrieval schemes [S4]. Next, the same efficiency calculation is carried out as a function of  $\gamma_s$  for the shortest possible storage time  $T \approx 2.5\tau_{\text{FWHM}}$ , as plotted in Fig. 2e, demonstrating the possibility of implementing a workable memory with ATS scheme under limited experimental conditions.

### EIT memory

For the EIT memory scheme, the calculations are performed for Gaussian input signals and shape-optimized write control fields, following the procedures described in Refs. [S2, S4]. For consistency, the shape of the read-out fields is set as the time-reversed shape of the write fields, although it does not necessarily have to be that.

In the analyses presented in Fig. 2c, for reference, the optimal memory efficiency as a function of optical depth is calculated in the native EIT regime with a long signal pulse  $\tau_{\text{FWHM}} \approx 20/\gamma_e$  such that the adiabaticity condition  $d\tau_{\text{FWHM}}\gamma_e > 40$  is fulfilled for all optical depth values of interest ( $d \geq 2$ ), as shown with dashed line. Notably, this curve for optimal EIT overlaps with the curve for optimal ATS (but with completely different bandwidth regimes), which is again in agreement with the

universal bounds found by Gorshkhov et al. [S3]. In these simulations, the strength and shape of the control Rabi frequency is optimized to minimize the signal lost through both absorption and leakage, noting that as absorption increases, leakage decreases and vice versa. The optimal peak Rabi frequency is found to be  $\Omega_c = 0.35\Gamma$  for  $d=10$ , which provides fractional delay of  $T_{\text{delay}}/\tau_{\text{FWHM}} \approx 2$  with minimal absorption and leakage for the constant control case (no complete halt of signal). As optical depth is increased, the peak Rabi frequency is also increased according to  $\Omega_c \propto \sqrt{d}$  in order to maintain the fractional delay. For optimal storage and retrieval, the shape of the Rabi frequency profile is optimized by setting smooth switch on/off such that the adiabatic evolution is preserved until the signal is completely stopped and reconstructed, as described in Refs [S3, S6].

For the storage and recall of a short signal pulse with  $\tau_{\text{FWHM}} = 0.1\gamma_e$  ( $B_{\text{FWHM}} = 13.5\Gamma/2\pi$ ), memory efficiency vs. optical depth is calculated in the backward recall scheme as presented in Fig. 2c. In this regime, as the slow-light effect is mediated by the dispersion through the ATS lines, the ATS splitting needs to be significantly larger than the signal bandwidth in order to avoid absorption that may lead to spontaneous emission or non-optimized ATS storage with distorted output. We find that  $\Omega_c/2\pi \approx 3B_{\text{FWHM}} = 40\Gamma/2\pi$  leads to the fractional delay  $T_{\text{delay}}/\tau_{\text{FWHM}} \approx 2$  and provides optimal storage/retrieval at  $d = 400 - 600$  by satisfying the adiabaticity condition as  $d\tau_{\text{FWHM}}\gamma_e = 40 - 60$ , which is in agreement with the results of Ref. [S4]. We also notice that the shape optimization of the control is more sensitive in the short-pulse regime. Therefore, the slope of the falling and rising edge of the write and read-out Rabi frequency is optimized for each optical depth [S4, S6]. In addition, as a consistency check, the excitation probability of the atomic polarization ( $|P|^2$ ) in the writing and reading stages is calculated for EIT and ATS-based storage/retrieval at  $d = 600$ , yielding the same memory efficiency  $\approx 0.9$  for both schemes. We find that the EIT-based storage results in six times smaller probability of polarization excitation than the ATS storage, showing that the atomic polarization is, to a great extent, adiabatically eliminated with this storage scheme.

In Fig. 2d, the scaling of optical depth with respect to signal bandwidth ( $B_{\text{FWHM}} \gg \Gamma/2\pi$ ) is analyzed for near-optimal memory efficiency  $\eta > 0.85$  at the limit of the adiabaticity condition. Following a similar procedure described for ATS memory, for a given  $\tau_{\text{FWHM}} \ll 1/\gamma_e$ , optimal optical depth is determined from the limiting adiabatic operation condition  $d\tau_{\text{FWHM}}\gamma_e \approx 50$ . For these optical depths, it is numerically verified in the range  $B_{\text{FWHM}} = 7\Gamma/2\pi$  to  $110\Gamma/2\pi$  that the efficiency is always maintained as  $\eta \approx 0.85 - 0.97$  with the same system dynamics. In this bandwidth scaling, the peak Rabi frequency of the control fields is changed proportionally to the signal bandwidth to maintain the fractional delay  $\approx 2$  and hence optimal efficiency, yielding a curve for peak control power ( $\mathcal{P} \propto \Omega_c^2$  in normalized units) vs.



bandwidth in the inset of Fig. 2d.

Finally, as shown in Fig. 2e we analyze EIT memory efficiency vs. spin decoherence in the parameter regime very similar to our experimental conditions:  $\tau_{\text{FWHM}} = 300$  ns,  $\Omega_c/2\pi = 2.4$  MHz,  $d = 3.5$ ,  $\gamma_e/2\pi = 3$  MHz and  $\gamma_s/2\pi < 5$  MHz. Under these conditions, with  $\gamma_s/2\pi = 0$  and optimized control shape, the optimal efficiency of EIT memory is numerically found to be  $\eta \approx 20\%$ , by satisfying the adiabatic operation condition  $d\tau_{\text{FWHM}}\gamma_e \approx 20$  for the forward recall. Note that this efficiency value is nearly the same as the universal optimal efficiency for  $d = 3.5$  for both forward and backward recall [S3]. Next, the same calculation is performed as a function of  $\gamma_s$  for the shortest possible storage time  $T \approx 2.5\tau_{\text{FWHM}}$ , as plotted in Fig. 2e. In contrast to the trend that is observed for ATS memory, EIT memory efficiency decreases substantially as  $\gamma_s$  is increased, and eventually approaches zero at  $\gamma_s/2\pi \rightarrow 0.4$  MHz, which is the case in our experiments. Finally, to verify that shorter signal durations are non-optimal for EIT storage in this regime, memory efficiency is calculated for input signals with different durations  $\tau_{\text{FWHM}} < 300$  ns using the same optimized control shape but with a peak Rabi frequency adapted to each signal duration. We confirm that the efficiency deviates further from the optimal efficiency value of 20% as the signal pulse is shortened. Particularly, in the regime that  $\tau_{\text{FWHM}} < 100$  ns, this degradation becomes substantial due to the break-down of adiabaticity, which also makes ATS-based storage the unavoidable choice for reaching optimal efficiency.

### Off-resonant Raman memory

For the off-resonant Raman memory scheme, the calculations are performed for Gaussian input signals and optimized write and read-out control fields, following the procedures described in Refs. [S7, S8] which customize this scheme particularly for broadband storage under limited control power conditions (balanced light-assisted and matter-assisted coupling regime). For optimal storage, in addition to satisfying the general condition  $d\tau_{\text{FWHM}}\gamma_e \gg 1$ , adiabaticity is ensured by far-off-resonant operation (Raman condition) such that  $\Delta \gg \gamma_e$  and  $\Delta > (\Omega_c, B_{\text{FWHM}})$  with limited Rabi frequency, where  $\Delta$  is the detuning of signal and control field from the excited level  $|e\rangle$ .

In the analyses presented in Fig. 2c, efficiency vs. optical depth for the storage and recall of the signal pulse with  $B_{\text{FWHM}} = 13.5\Gamma/2\pi$  ( $\tau_{\text{FWHM}} = 0.1\gamma_e$ ) is calculated in the backward recall scheme with  $\Omega_c/2\pi \approx 3B_{\text{FWHM}} = 40\Gamma/2\pi$  (peak Rabi frequency of the write field) and  $\Delta = 67.5\Gamma$ , fulfilling the Raman conditions.

Near-optimal memory efficiency ( $\eta \approx 0.85$ ) is reached at  $d = 600$  by satisfying the general adiabatic condition as  $d\tau_{\text{FWHM}}\gamma_e \approx 60$ , similar to the EIT scheme. The control field optimization is performed separately for the write and read-out fields, as detailed in [S7]. The timing of the write field with a Gaussian profile is set to be earlier with respect to the signal, in order to compensate the fast-light propagation effect induced by a negative dispersion due to the Raman absorption feature. In addition, the duration of the write field is adjusted to be longer than the signal, which enhances the coupling by increasing the control pulse energy. These optimizations are performed iteratively until the Raman absorption, and thus storage efficiency, is maximized. For the retrieval stage, a Gaussian-shaped control pulse, which is longer than the signal, is used with significantly larger peak Rabi frequency than the write pulse. We find that 2-3 times larger Rabi frequency is sufficient for optimal retrieval, leading to  $\Omega_c = 90\Gamma$  at the read-out, which is also consistent with the results of Ref [S7]. We note that in our analysis although efficiency vs. optical depth for Raman memory exhibits a very similar trend to that for EIT memory due to their common adiabatic operation, the efficiency for each  $d$  is 5% – 15% smaller than the EIT in the range  $100 < d < 800$ . In this case, to ensure that our Raman storage/retrieval is well-optimized, we cross-check our optimal efficiency and optimal parameter values with the ones determined by Nunn et al. [S8] for the same signal bandwidth ( $B_{\text{FWHM}} = 13.5\Gamma$ ). We find that while our optimal parameters ( $\Delta = 67.5\Gamma$  and  $\Omega_c = 40\Gamma$  for the write) are similar to theirs ( $\Delta = 75\Gamma$  and  $\Omega_c = 50\Gamma$  for the write), our optimal memory efficiency ( $\eta = 0.83$ ) is reasonably close to theirs ( $\eta = 0.89$ ) for the same optical depth ( $d = 600$ ).

In Fig. 2d, scaling of optical depth with respect to signal bandwidth ( $B_{\text{FWHM}} \gg \Gamma/2\pi$ ) is analyzed for near-optimal memory efficiency  $\eta \approx 0.85$  at the limit of the adiabaticity condition. Following the previously described procedure for ATS and EIT memory, for a given  $\tau_{\text{FWHM}} \ll 1/\gamma_e$ , optimal optical depth is determined from the limit adiabatic operation condition  $d\tau_{\text{FWHM}}\gamma_e \approx 60$ . For these optical depth values it is numerically verified in the range  $B_{\text{FWHM}} = 7\Gamma/2\pi$  to  $110\Gamma/2\pi$  that the efficiency is always maintained as  $\eta \approx 0.85$  with the same system dynamics. In this analysis, the peak Rabi frequency of the control fields and the detuning are changed proportionally to the signal bandwidth in order to maintain the Raman conditions and effective coupling  $C$  (as defined in Methods), yielding a curve that shows the peak power requirement for Raman read-out ( $\mathcal{P} \propto \Omega_c^2$  in normalized units) vs. bandwidth in the inset of Fig. 2d.

---

[S1] Cho, Y-W. et al. Highly efficient optical quantum memory with long coherence time in cold atoms. *Optica* **3**,

- [S2] Hsiao, Y-F. et al. Highly Efficient Coherent Optical Memory Based on Electromagnetically Induced Transparency *Phys. Rev. Lett.* **120**, 183602 (2018).
- [S3] Gorshkov, A. V., André, A., Sørensen A. S., Lukin, M. D. Universal Approach to Optimal Photon Storage in Atomic Media *Phys. Rev. Lett* **98**, 123601 (2007).
- [S4] Gorshkov, A. V., André, A., Lukin, M. D. & Sørensen, A. S. Photon storage in  $\Lambda$ -type optically dense atomic media. II. Free-space model. *Phys. Rev. A* **76**, 033804–25 (2007).
- [S5] Gorshkov, A. V., André, A., Lukin, M. D. & Sørensen, A. S. Photon storage in  $\Lambda$ -type optically dense atomic media. III. Effects of inhomogeneous broadening. *Phys. Rev. A* **76**, 033806 (2007).
- [S6] Phillips, N. B., Gorshkov, A. V., and Novikova, I. Optimal light storage in atomic vapor. *Phys. Rev. A* **78**, 023801 (2008).
- [S7] Nunn, J. et al. Mapping broadband single-photon wave packets into an atomic memory. *Phys. Rev. A* **75**, 011401-R (2007).
- [S8] Nunn, J. Quantum Memory in Atomic Ensembles. *PhD Thesis*, Chapters 4-7 University of Oxford. (2008).